

Fermi surface and topology of multiband superconductor BeAu

Riccardo Vocaturo,¹ Klaus Koepernik,¹ Dániel Varjas,^{1,2,3} Oleg Janson,¹ Maia G. Vergniory,^{4,5,6} and Jeroen van den Brink^{1,2,7}

¹*Leibniz Institute for Solid State and Materials Research (IFW) Dresden, Helmholtzstrasse 20, 01069 Dresden, Germany*

²*Würzburg-Dresden Cluster of Excellence ct.qmat, Helmholtzstrasse 20, 01069 Dresden, Germany*

³*Department of Theoretical Physics, Institute of Physics,*

Budapest University of Technology and Economics, Műegyetem rkp. 3., 1111 Budapest, Hungary

⁴*Regroupement Québécois sur les Matériaux de Pointe (RQMP), Quebec H3T 3J7, Canada*

⁵*Donostia International Physics Center, 20018 Donostia-San Sebastian, Spain*

⁶*Département de Physique et Institut Quantique,*

Université de Sherbrooke, Sherbrooke, J1K 2R1, Québec, Canada.

⁷*Institute of Theoretical Physics, Technische Universität Dresden, 01062 Dresden, Germany*

(Dated: March 9, 2026)

The chiral material BeAu was recently identified as a multiband type-I superconductor with a critical temperature of 3.2 K. As a member of the B20 crystal family (space group $P2_13$), its band structure hosts multifold fermions at high-symmetry points, unpaired Weyl points and even nodal surfaces. This renders BeAu an appealing system to investigate the interplay between superconductivity and topology. Here we present a comprehensive first-principles analysis of BeAu's electronic structure focusing on its Fermi surface's topology and the implications for superconductivity. Together with the presence of four- and six-fold fermions at high-symmetry points, we identify several additional isolated Weyl points near the Fermi level. We also determine the associated topological edge states—the surface Fermi arcs. Computing the Chern number associated to different Fermi surface sheets, we show that BeAu harbors a $\nu = 4$ topological superconducting phase in the presence of s -wave pairing of alternating sign (s_{\pm} pairing). Notably, we also identify a Fermi surface with a Chern number of +6; the highest value reported to date. Finally, our analysis reveals strong inhomogeneity in the orbital character of electronic states at the Fermi level, suggesting a link to the observed multigap superconductivity.

I. INTRODUCTION

The family of B20 compounds has been gaining significant attention in recent years, presenting itself as a natural platform for investigating exotic topological phases [1]. Materials belonging to this family crystallize in the FeSi-type lattice, with chiral space group $P2_13$ (no. 198). This structure is characterized by the absence of inversion as well as mirror symmetries, and the presence of 3 screw-rotation axes along the unit cell's main diagonals. Such uncommon combination of crystalline symmetries provides ideal conditions for realizing unconventional electronic features in the band structure. For instance, symmetry-enforced multiband crossings occur at high-symmetry points in the Brillouin zone (BZ), carrying topological charges as large as five [2]. These crossings, termed multifold fermions [3, 4], have been extensively studied in recent years due to the possibility to yield extremely long surface Fermi arcs [5], second-harmonic generation [6, 7], quantized circular photogalvanic effect [8], and many more (non-linear) transport properties [9–12].

Yet, multifold fermions are not the only unconventional features in chiral crystals. For example, space group 198 is among the few known cases where nodal surfaces (NS) and isolated Weyl points (WPs) can be found. Here, these two elements appear together and make it possible to circumvent the famous Nielsen–Ninomiya theorem, allowing the existence of a single WP in a periodic lat-

tice. These types of excitations were first proposed in 2019 [13, 14] and experimentally observed two years later in another B20 compound, PtGa [15].

Another aspect of great interest lays in the appealing prospect of realizing topological superconductivity. Qi *et al.* [16] showed that time-reversal-invariant Weyl semimetals can undergo a topological superconducting transition if the pairing function changes sign between Fermi surfaces (FSs) of different chirality. In the weak-coupling limit, the topological invariant is given by:

$$\nu = \frac{1}{2} \sum_{i \in FS} C_i \operatorname{sgn}(\Delta_i) \quad (1)$$

where Δ_i is the superconducting gap on the i -th FS, and C_i is its Chern number, computed as the flux of Berry curvature through the i -th sheet. In a conventional Weyl semimetal, $C_i = \pm 1$ for Fermi surfaces enclosing a Weyl point and zero otherwise. While a sign-changing order parameter is not typically expected in conventional electron-phonon superconductors, Hosur *et al.* [17] showed that second-order effects from Coulomb repulsion between different FSs can stabilize such a state, even in the presence of purely local interactions. In this context, B20 compounds are interesting because they host multifold fermions at high-symmetry points, giving rise to extended and well-separated Fermi surfaces with large Chern numbers. Contrary, in conventional Weyl semimetals, WPs are usually located close to one another, resulting in a smaller probability to observe a

sign change of the superconducting gap across the corresponding pockets. Significant attention has thus been devoted to the effect of superconductivity on the multi-fold fermions at the Γ and R points [18–20]. In minimal toy models, it has been predicted that s_{\pm} pairing may even drive a topological superconducting transition with invariant $\nu = 4$ [21].

In this work we turn our attention to BeAu, which, remarkably, exhibits a superconducting transition $T_c \approx 3.2$ K [22–24], despite the poor superconducting properties of both beryllium and gold. It is also one of only two known superconductors in the B20 family (the other being RhGe [25]). Additionally, multiple experimental evidence points toward the presence of multiband superconductivity this system [26–28].

The agreement between the experimentally observed T_c and theoretical calculations [29] suggests that superconductivity in BeAu is primarily driven by electron-phonon coupling from light Be atoms; a mechanism reminiscent of high-pressure hydrides. However, the presence of two distinct superconducting gaps leaves two important questions unanswered: which FSs are involved, and what mechanism gives rise to their different gap magnitudes? Experimental data further hints that one of the gaps is strongly coupled while the other is weakly coupled [29], pointing towards a significant anisotropy in the interaction strength. This raises the possibility that an s_{\pm} pairing may emerge despite the dominance of electron-phonon coupling, leading to a topological superconducting phase.

Since previous theoretical studies [21] were conducted at the effective model level, inevitably neglecting material-specific aspects, we present here a comprehensive first-principles investigation of the electronic structure of BeAu, with a particular focus on its Fermi surface. After a general overview of the crystal (Sec. II) and electronic (Sec. III) structure we highlight the presence of known multifold fermions at the high-symmetry points (Sec. III A) and perform a systematic search throughout the BZ to identify WPs at generic positions, finding multiple *isolated* crossings in the proximity of the Fermi level (Sec. III B). We also examine in depth the surface spectral properties, discussing important aspects which have not been considered in a recent study [30]. In Sec. IV and Sec. V, we focus on the complex Fermi surface of this system, revealing additional electron and hole pockets beyond those at Γ and R points captured by the effective model in Ref. [21]. Moreover, the presence of several isolated crossings in the proximity of the Fermi level complicates the determination of the topological charge of each sheet, which is not easily inferred from a counting argument alone. Consequently, to rigorously confirm the possibility of a non-trivial topological invariant in the presence of s_{\pm} superconductivity, we carry out a careful numerical computation of Fermi-surface Chern numbers.

Our main result is a complete topological characterization of the Fermi surface of BeAu, showing that it is consistent with the $\nu = 4$ topological superconducting phase

theoretically proposed in minimal models [20, 21]. We also identify a Fermi surface sheet with a Chern number of $C = 6$ which could, in principle, support even richer superconducting phases. To the best of our knowledge, this is also the highest value reported for a single Fermi surface. Finally, we find a highly anisotropic distribution of atomic orbital character at the Fermi level, a factor that could influence the electron-phonon interaction and help explain the origin of the observed multigap behavior.

II. CRYSTAL STRUCTURE

The low-temperature phase of BeAu emerges below 860 K [24], crystallizing in the chiral FeSi-type structure with the cubic unit cell parameter $a = 4.6699(4)$ Å at room temperature [22]. This structure type features sevenfold coordination polyhedra and represents an approximation to icosahedral quasicrystals [31].

The crystal structure belongs to the well-known space group $P2_13$ (No. 198), which is chiral due to the absence of both inversion symmetry and mirror planes. Its symmetry operations include a C_3 rotational axis along the [111] direction and three non-symmorphic screw rotations: $\{2_1(100) \mid \frac{1}{2}\frac{1}{2}0\}$, $\{2_1(010) \mid 0\frac{1}{2}\frac{1}{2}\}$, and $\{2_1(001) \mid \frac{1}{2}0\frac{1}{2}\}$. In this work, we will refer to such screw rotations with the notation \tilde{C}_i with $i = x, y, z$. As structural input for our calculations, we use the experimental room-temperature structure where Au and Be occupy the $4a$ Wyckoff positions with coordinates $x_{\text{Au}} = 0.8549$ and $x_{\text{Be}} = 0.15$ [22].

III. ELECTRONIC STRUCTURE

To study the electronic structure of BeAu, we performed full-relativistic density functional theory (DFT) calculations using the full-potential local-orbital code FPLO [32] version 22.01-63. For the exchange-correlation term, we employed the generalized gradient approximation (GGA) [33]. The BZ was sampled by a $12 \times 12 \times 12$ mesh of k -points. For slab calculations, a suitable Wannier representation was obtained through the dedicated FPLO module [34]. To do so, Kohn-Sham eigenstates were projected onto a basis of 80 spinfull orbitals that comprises Be $2s$, $2p$ and Au $6s$, $5d$; in an energy window between -9 and 5 eV.

The band structure with and without spin-orbit coupling (SOC) is shown in Fig. 1 (a) while in Fig. 1 (b) we resolve atomic contributions of each band at each momentum. The density of states (DOS) have been previously published in Ref. [22, 29]. In particular, in [29], it was shown that Be and Au atomic contribution are essentially equal around E_F . This is consistent with Fig. 1 (b), indicating strong hybridization of valence electrons in this compound. However, the atomic-resolved band structure evidences quantitative difference in the orbital character of some states. For instance, the hole pocket

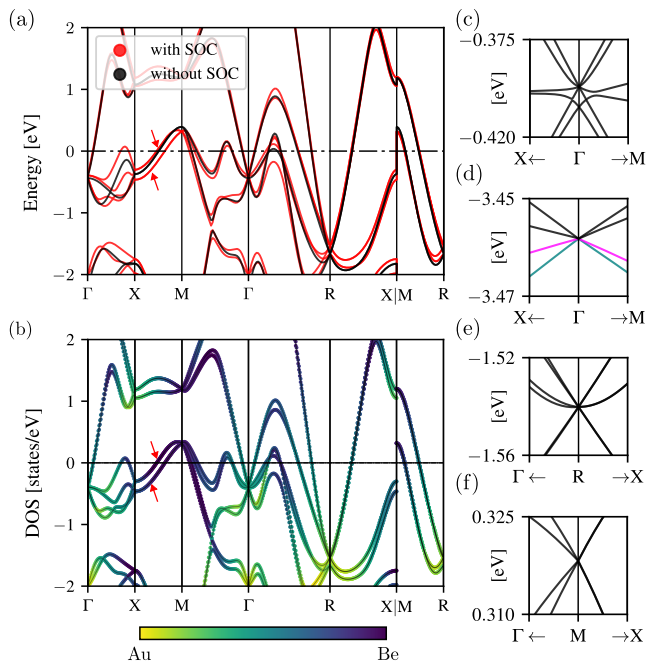


FIG. 1. (a) Scalar- (without SOC) and full-relativistic (with SOC) GGA band structures of BeAu. (b) Atomic-resolved full-relativistic band structure, highlighting the relative Au and Be contributions. (c-f) Zoom-in on the multifold band crossing at high-symmetry points carrying non-trivial Chern numbers (full-relativistic band structure). In (d) we color in pink the band carrying $C = 5$ (see discussion in the main text for details).

around the M point has a remarkably higher Be contribution with respect to the neighbouring bands crossing the Fermi level.

The impact of SOC can also be understood comparing Fig. 1 (a) to the orbital-resolved band structure in panel (b). As expected, Be, being a light element, induces negligible effects, while much wider band splitting are associated with regions of the BZ with stronger Au contribution. For instance, comparing Γ -M and M-X paths, we observe that along Γ -M, where Be character dominates, the SOC-induced splitting is smaller. As we move toward Γ along the Γ -X direction, the splitting increases, in line with a higher Au contribution. In Ref. [30], the weaker spin-orbit splitting of Be-dominated states was invoked to explain the lower spin-Hall conductivity of this material compared to the Weyl semimetal TaAs or the conventional metal Pt. However, the same study also identified a significant amount of spin Berry curvature near the Fermi level, which results in a much higher spin-Hall conductivity relative to other B20 compounds.

A. Topological multifold crossings and Fermi arcs

The band structure of BeAu features multiple examples of exotic crossings which are not encountered in conventional Weyl semimetals and that are enforced by the symmetries of the crystal.

While conventional WPs are described by a local Hamiltonian which is adiabatically connected to $H_{\mathbf{k}} = \boldsymbol{\sigma} \cdot \mathbf{k}$, the presence of additional crystalline symmetries allows the generalization to higher dimensional intersections. Such objects will be described by an Hamiltonian of the form $H_{\mathbf{k}} = \mathbf{S} \cdot \mathbf{k}$ with $\mathbf{S} = (S_x, S_y, S_z)$ being some n -dimensional (iso)spin matrices.

B20 compounds have been shown to host 4-fold degenerate crossings at the time-reversal-invariant momenta (TRIM) Γ and 6-fold ones at R, with chiral charge of -4 and $+4$ respectively [18, 30, 35, 36]. Here, we find them at -0.4 eV (at Γ) and at -1.5 eV (at R), in agreement with Ref. [30]. We further confirm the value of the topological charge by explicitly integrating the Berry curvature over a small surface centered around such crossings. These ± 4 Weyl fermions give rise to four surface Fermi arcs connecting Γ to the projection of R onto the two-dimensional (2D) surface BZ (denoted by \bar{M}). The arcs can be visualized by computing the surface spectral function on the (001) termination. Fig. 2 shows the results for different energy cuts starting from the Fermi level (a) up to 0.2 eV above it (e). The best resolution of the arcs is achieved at higher energies, Fig. 2(e), where fewer bulk bands are present: very long states originating from $\bar{\Gamma}$ and following a complex trajectory culminate in a “spiraling” behavior near \bar{M} . Their connectivity becomes clear if the plot is extended to the neighboring BZ. Contrary, at the Fermi level, the arcs strongly hybridize with the surrounding states, and they become hard to track.

To gain deeper insight into the physics of the arcs we examine their evolution as a function of energy. We observe three key features, each marked by a different colored arrow in Fig. 2. Starting from 0.2 eV, the first feature appears around 0.15 eV: it corresponds to the opening of the circular surface states at the \bar{X} point, the red arrow in panel (d). Simultaneously, the long arcs around \bar{M} are pushed downward, signaling the onset of a connectivity exchange between the two. This process continues down to approximately 0.10 eV, where the inner circle around \bar{X} also breaks open (blue arrow). At 0.06 eV, the arcs originally stemming from the right side of $\bar{\Gamma}$ are now attached to the spectral weight around \bar{X} , rather than connecting to \bar{M} . At this point, it is necessary to comment on the additional spectral weight near \bar{X} . These supplementary surface states also originate from the same Fermi arcs connecting $\bar{\Gamma}$ to \bar{M} : their strong dispersion in this compound causes them to cross the Fermi level multiple times. A similar behavior is theoretically predicted for GeRh [18], but here the effect appears to be significantly more pronounced. In panel (f) we also show the spin character of these surface states. We observe an avoided crossing along the \bar{X} - \bar{Y} direction: the less dis-

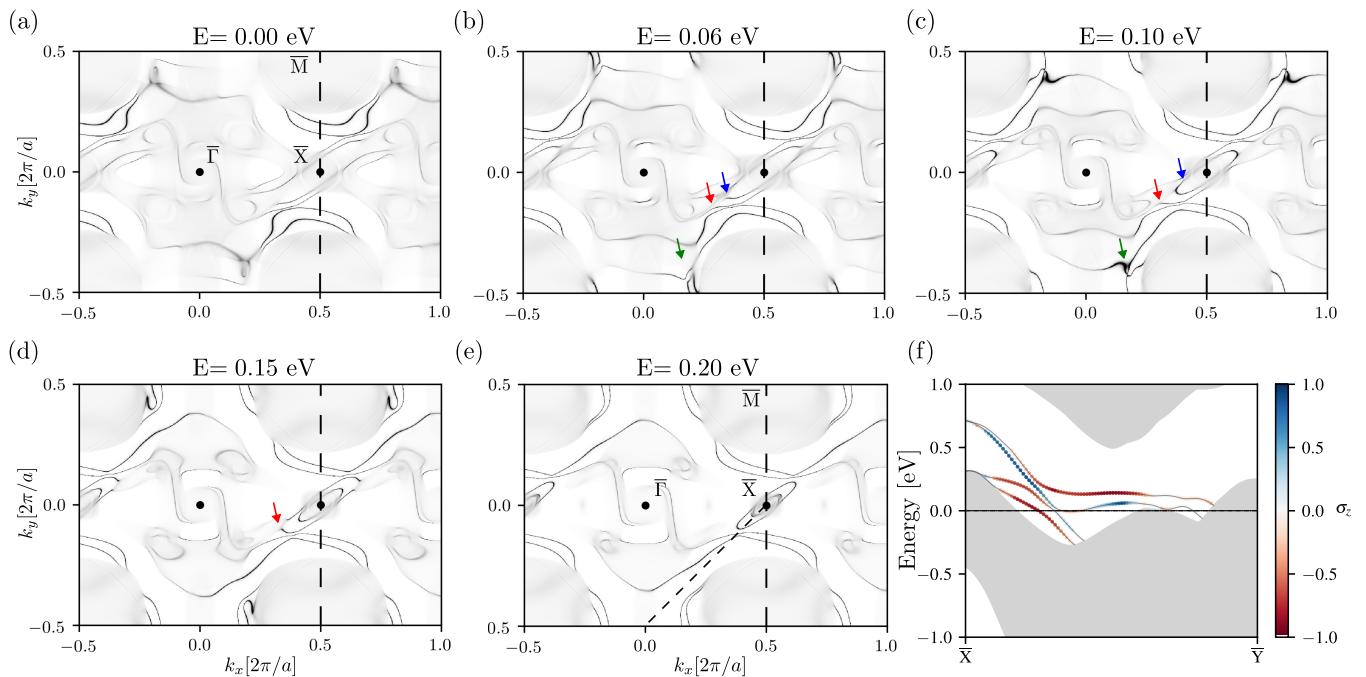


FIG. 2. Spectral function $A(\mathbf{k}, \omega)$ at fixed energy, evaluated at a depth of 10 Bohr radii (5.29 Å) for the (001) surface termination. In panel (a), $A(\mathbf{k}, \omega)$ is shown at the Fermi level, while panels (b), (c), (d), and (e) correspond to $\omega = 0.006, 0.10, 0.15,$ and 0.2 eV, respectively. The red, green, and blue arrows highlight the change of connectivity between Fermi arcs, as discussed in the main text. Panel (f) displays the band structure of a 10-layer slab along the dashed path indicated in panel (e). Bulk states are shown in gray, while surface states are colored according to the expectation value of \hat{S}_z . We define a surface state as a band whose atomic weight on the first layer exceeds 30%. Surface states associated with the opposite termination are not shown.

persive arcs with strong spin-down (red) components are “separated” by the more dispersive spin-up (blue) state.

Lastly, another connectivity exchange takes place around 0.10 eV, which we indicate with the green arrow in Fig. 2(b-c). This process is accompanied by the formation of a U-shaped structure with significant spectral weight, clearly visible in panel (c). An analogous behavior has been reported to occur also in RhSi, and it was found to realize type-II (surface) van Hove singularities [37]. It is therefore reasonable to expect the emergence of the same type of singularity in our case. Although we did not explore this aspect further in the present work, it certainly warrants further examinations. Recent experimental [38] and theoretical [39–42] studies have shown that Fermi arcs can be highly sensitive to superconducting instabilities, leading to critical temperatures significantly higher than those observed in bulk crystals. Therefore, BeAu is a promising candidate to further investigate such phenomenon, given the very large size of the arcs and the potential presence of van Hove singularities.

At this point, we observe that our surface state spectra are broadly consistent with the earlier results of Ref. [30], though some discrepancies are present. We attribute these differences to the choice of structural inputs for the DFT calculations (our use of experimentally determined

lattice constants and Wyckoff positions versus the DFT-optimized structure in Ref. [30]) as well as the possibility of a different (unspecified) energy shift in the latter work.

In addition to the just discussed $|C| = 4$ fermions, BeAu exhibits another type of multi-fold band crossing near the Fermi level, Fig. 1(f). This crossing is located at the TRIM point M, around 0.32 eV, and is referred to as a *double WP* or *charge-2 Dirac point* (DP). We will use the latter term throughout. It comprises two overlapping WPs of the same chirality, resulting in a total topological charge of two. Its existence stems from the presence of screw-rotation symmetries and time-reversal symmetry (\mathcal{T}). As discussed later in Sec. III B, the combined action of \tilde{C}_i and \mathcal{T} enforces a two-fold degeneracy along the boundary of the BZ. Consequently, at the TRIM point M, a four-fold degeneracy must occur. A numerical analysis of the Wannier bands confirms that all crossings at the M point are indeed charge-2 DPs. The one closest to the Fermi level carries a topological charge of $C = -2$. Remarkably, the charge-2 DP at M does not give rise to additional surface Fermi arcs (see Sec. III B).

We conclude this section by discussing another degeneracy 3.5 eV below the Fermi level, which deserves mentioning as it constitutes the only known case where a band crossing can carry a topological charge of five. Originally, Bradlyn *et al.* [3] argued that the maximum

Chern number permitted by crystalline symmetries originates from a 4-fold crossing adiabatically connected to the spin-3/2 Hamiltonian, yielding $|C| = 4$ at half-filling. More recently, Alpin *et al.* [2] showed that in space groups 195 and 199, a 4-fold crossing can exist that is *not* adiabatically connected to the spin-3/2 model, allowing Chern numbers of $(3, -5, +5, +3)$ for the respective bands. However, the $C = \pm 5$ bands are always paired with the ones carrying $C = \mp 3$, so the net topological charge at half filling remains ± 2 , preserving the effective upper bound of $|C| = 4$. In Fig. 1, panel (d), we color the band with $C = -5$ in purple and the band with $C = +3$ in green. A similar 4-fold crossing occurs at even lower energies.

B. Unpaired Weyl crossings

Since periodicity requires that no net flux of Berry curvature crosses the surface of the BZ, nodes with equal and opposite chirality usually come in pairs, resulting in an overall net chirality of zero. To satisfy the condition of zero net Berry curvature flux across the BZ while permitting an isolated WP, a compensating source or sink of Berry curvature must exist. In certain chiral crystal structures, rather than a partner WP, this role is played by *nodal walls*: symmetry-protected nodal surfaces [13] that reside on the boundary of the BZ.

In such systems, the conventional picture of Weyl semimetals as stacks of 2D Chern insulators in reciprocal space becomes inadequate. Due to the presence of nodal surfaces at *all* BZ boundaries, no 2D slice of the three-dimensional BZ exhibits a full band gap. Consequently, the existence of a partner node is no longer required as the zero net-flux condition is met because of the nodal walls. Similarly, bulk-boundary correspondence breaks down, and such isolated WPs are not accompanied by topologically protected surface states [14].

In BeAu, the combination of time-reversal symmetry and skew rotations pins the nodal degeneracies at the edges of the BZ, hence the name nodal walls. This is because $(\mathcal{T}\tilde{C}_i)^2 = -e^{-i\mathbf{k}\cdot\mathbf{t}_i}$, where \mathbf{t}_i refers to a translation along i . Thus, Kramers' degeneracies are guaranteed at all $k_i = \pi$ planes since $(\mathcal{T}\tilde{C}_i)^2 = -1$. These degeneracies can be seen in the band structure shown in Fig. 1(a-b), for example, along the M-X path. We marked them by red arrows for convenience. Note that as one moves away from the BZ boundary towards the interior (e.g., along Γ -M), the bands split again. It is important to stress that only the bands merging into these nodal walls can host unpaired WPs. For instance, the fourfold-degenerate fermions at Γ and R originate from bands not joined by nodal walls and thus behave as conventional pairs of Weyl nodes with associated surface Fermi arcs III A.

The unpaired crossings can be conventional Weyls or even multi-fold fermions and can occur both at high-symmetry points—such as the charge-2 Dirac point at

M—as well as at generic points in reciprocal space. To systematically explore their distribution, we performed a dense-mesh scan of the full BZ. Since there is no gap in the energy spectrum up to several eV from the Fermi level, we restricted our attention to the bands which intersect the Fermi level, identifying 81 WPs in the irreducible octant of the first BZ. We report in Fig. 3 (c) the energy and positions of six unpaired WPs found within an energy window of 50 meV. Their projection onto the $k_x k_y$ -plane is also shown in panel (a) of the same figure.

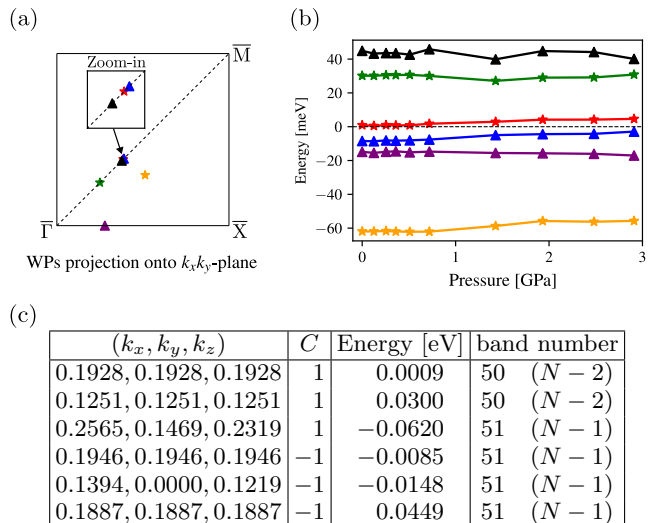


FIG. 3. Unpaired WPs at generic k -points in the energy window of $\sim \pm 50$ meV around the Fermi level. (a) Projection onto the $k_z = 0$ plane of the WP positions belonging to the irreducible BZ. The asterisk (triangle) marks correspond to positive(negative) chirality. (b) WPs' energy dependence on external pressure. (c) Exact 3-dimensional position (units of $2\pi/a$) of the nodes, with corresponding energy and chirality. The “band number” refers to our Wannier-projected Hamiltonian. We further label the same bands according to the order in which they appear at the four-fold fermion at Γ in Fig. 1(a): $N + 2$ corresponds to the highest eigenvalue.

In Fig. 3 (b), we show the energy dependence of the crossings under applied pressure, which remains largely unchanged up to 3 GPa. This behavior aligns with the minimal variation observed in the DOS reported in the literature [29]. To determine the crystal structure at different pressures, we used the experimental curves for the lattice parameter a as a function of pressure from Ref. [29] and performed scalar-relativistic symmetry-constrained relaxation of the atomic coordinates. This step was essential because even tiny changes in the crystal structure have a significant impact on the energy of the nodes. For example, the WP at -0.062 eV in our plot lies outside the energy range of ± 50 meV, however, using the value of $a_0 = 4.6699$ Å from Ref. [22] yields roughly -0.040 eV.

IV. FERMI SURFACE

In this section we present a detailed analysis of the Fermi surface of BeAu focusing on the topological charge carried by each part of the surface. Our motivation is twofold. First, the presence of unconventional crossings, we find, leads to Fermi sheets carrying unexpectedly high topological charge. Second, this quantity, also referred as the Chern number of a sheet, together with the sign of the superconducting gap characterizes the topology of a time-reversal invariant superconductor via Eq. (1) [16, 17].

First of all, we present the Fermi surface in Fig. 4, which is highly complex, featuring numerous nested as well as intersecting sheets. We label each one increas-

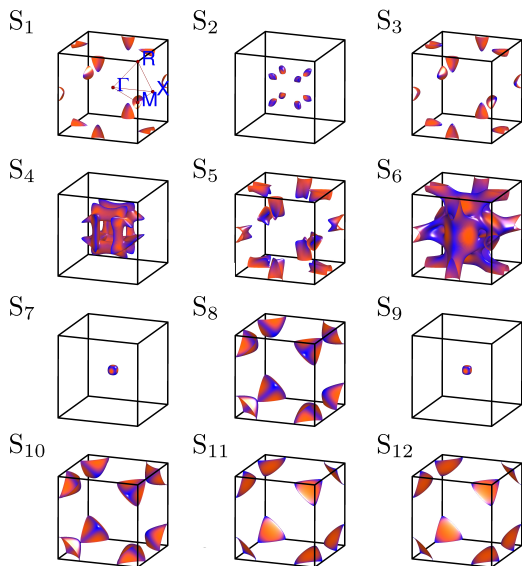


FIG. 4. All full-relativistic Fermi surfaces of BeAu computed with GGA and SOC with the de Haas-van Alphen module of FPLO. We used a $24 \times 24 \times 24$ k -mesh with additional 3 bisections. The color gradient represents the Fermi velocity intensity (units not shown), ranging from low (blue) to high (orange) values.

ingly from 1 to 12 in the order shown in the figure. In our notation, S_1 , S_3 , and S_5 each consist of three pockets, meaning they technically correspond to three distinct sheets for each plot. We group them together because they are symmetry-related. Around Γ , there are two small concentric and closed Fermi surfaces (S_7 and S_9), which become degenerate in the absence of SOC. An analogous situation arises near the R point, where, however, there are two pairs of intersecting surfaces ($S_8 \cup S_{10}$ and $S_{11} \cup S_{12}$). In this second case the spin-orbit splitting is hardly noticeable.

To characterize the Chern number of each sheet we perform a numerical integration to explicitly compute the

flux:

$$\begin{aligned} C_i &= \frac{1}{2\pi} \oint_{S_i} \Omega_i(\mathbf{k}) \cdot d^2\mathbf{k} \\ &= \frac{1}{2\pi} \oint_{S_i} \Omega_i(\mathbf{k}) \cdot \hat{\mathbf{n}}_i(\mathbf{k}) d^2k, \end{aligned} \quad (2)$$

where S_i denotes the fully connected i -th part of the Fermi surface and $\Omega_i(\mathbf{k}) = \nabla_{\mathbf{k}} \times \langle u_{i,\mathbf{k}} | i\partial_{\mathbf{k}} | u_{i,\mathbf{k}} \rangle$ is the Berry curvature evaluated at the surface S_i . The vector $\hat{\mathbf{n}}_i$ specifies the normal direction of the surface element $d^2\mathbf{k}$ and it points along the direction of the Fermi velocity. We further recall that when multiple surfaces intersect only the flux summed over all touching regions has physical significance and can be expected to be quantized.

In conventional Weyl semimetals, Eq. (2) can be evaluated implicitly, without explicit integration: a sheet enclosing a WP possesses a Chern number $|C| > 0$, whereas if no WPs are enclosed, the sheet has $C = 0$. This procedure, although still theoretically applicable here, becomes challenging due to the abundance of unpaired WPs and nodal surfaces.

To numerically perform the integration, we first obtain a fine triangulation of each surface S_i . Then the Berry curvature over each plaquette is obtained by averaging the values of $\Omega_i(\mathbf{k})$ at the three vertices. Finally, the normal vector $\hat{\mathbf{n}}_i$ is computed from the coordinates of the plaquettes' vertices with simple geometric rules. The main practical challenge in evaluating Eq. (2) arises for intersecting sheets. In such cases, two kind of errors become relevant when sampling the Fermi surfaces: (i) Wannier interpolation is not exact, and (ii) the Fermi surface is obtained by interpolating nearby points, so the k -points assigned to a given surface S_i do not strictly lie on the iso-energy contour. This introduces a small shift $\delta\mathbf{k}$, which propagates into the surface integral. These errors are typically negligible since $\Omega_i(\mathbf{k})$ varies smoothly, but near band touchings, where $\Omega_i(\mathbf{k})$ can change rapidly, even small shifts accumulate. The more degeneracies present, the greater the computational effort required to control them. To address this issue, we can move slightly away from the Fermi level, where problematic degeneracies are absent or easier to resolve. For instance, this approach was used to determine the Chern number of S_6 , which was particularly challenging. At just 0.1 eV above the Fermi level, the surface splits into eight pockets centered around X, which we could evaluate separately and then sum their contributions. Finally, since gauge invariance requires $\sum_{i \in \text{FS}} C_i = 0$ [43], the chirality can still be inferred from the sum rule in the case one part of the Fermi surface fails to converge.

The results are summarized with the table in Fig. 5. Interestingly, the flux through the Fermi sheets around Γ , R and M matches the value expected from the presence of multifold fermions sitting at the corresponding high-symmetry points, despite the presence of additional nearby crossings. The two sheets S_2 and S_4 present an extremely small gap, shown on the left of Fig. 5, which

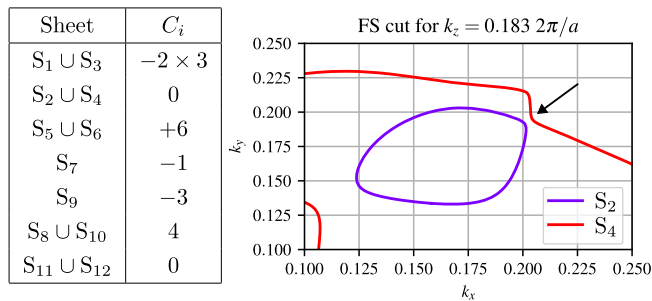


FIG. 5. On the left the table summarizes the Fermi surface’s Chern number as computed numerically from Eq. (2). In the first line we make explicit that S_1 and S_3 have multiplicity of 3 because there are 3 symmetry-related M points. For bookkeeping purposes, we have group them together in all previous plots. In the second line, we decided to group S_2 and S_4 together because it was too demanding to computationally resolve the very small band gap (shown on the right).

makes direct computation of the flux very sensitive to the mesh. Raising the energy slightly allows to better resolve the gap and we conclude (with a reasonable error of $\sim 0.37\%$) that both of them are trivial. However, for this conclusion to hold also at the Fermi level, we must know whether these bands intersect, not only at the Fermi level, but at all energies between 0 and 0.1 eV otherwise a possible redistribution of the topological charge is allowed. Given the very small size of the gap, the computational cost is high and we decided not to pursue this any further. At present, we can say for certain that $C_2 + C_4 = 0$.

V. IMPLICATIONS FOR SUPERCONDUCTIVITY

Now that all sheets have been characterized, we can comment on the effect of an s_{\pm} pairing state. To investigate the consequences of a sign change in the gap function, Huang et al. [21] assumed a functional form $\Delta(\mathbf{k}) \sim \sum_i \cos(k_i)$. This choice is not unique since any basis of the trivial representation (A) can be chosen— $\cos(k_i)$ being the simplest. While this choice is suitable for their effective model, it need not hold for BeAu.

In the absence of further experimental inputs, it is difficult to propose a well-motivated alternative, however, what is important for the appearance of a topological superconducting phase is a sign change between different Fermi surfaces; this could happen in a multi band superconductor if the Fermi sheets involved are, for example, the ones at Γ and R. Under this assumption, our numerical evaluation of the Fermi surface’s Chern number confirms that a topological superconducting phase with $\nu = 4$ can appear. We emphasize that numerically evaluating the surface Chern number was necessary due to the abundance of WPs located at generic positions, some even very close to Γ .

Although quite exotic, the presence of M pockets in theory enables the possibility of a different topological phase with $\nu = 6$. While such a phase may be unlikely to occur in BeAu due to the very small separation between S_6 and S_4 , similar electronic structures are common in B20 compounds, making this an intriguing possibility worth considering.

As a concluding remark, looking at the atomic-resolved band structure in Fig. 1, we can also conclude that S_5 and S_6 (centered at M) carry much more Be-character compared to the neighboring bands at the Fermi level. In Ref. [29], a simple model for the electron-phonon coupling involving only Be was proposed in order to explain the measured T_c . Given the good agreement with the experimental data, it is worth keeping in mind that the observed multi-gap formation could be linked to a non-uniform distribution of Be-character across the Fermi surface. In this case, however, a sign change between Γ and R becomes unlikely since the Γ and R point have comparable degree of atomic hybridization. On the other hand, the possibility of a sign change between Γ and M remains, yielding the previously mentioned $\nu = 6$ topological phase. Such phase was previously commented to be unlikely due to the small separation between the M pocket and other nearby Fermi surfaces but it could be possible. Then, a more involved choice of the basis function for the A-irrep must be invoked to described the s_{\pm} gap function. Further investigation, i.e. k -resolved electron-phonon calculations, are therefore necessary.

VI. CONCLUSIONS

In this work, we employed DFT combined with Wannierization to characterize the electronic structure of the chiral Weyl semimetal BeAu. This material belongs to the B20 family of compounds, which is known for featuring multi-fold band degeneracies with high Chern numbers. We first reviewed the band structure of BeAu and identified the presence of $C = 4$ multifold fermions at the Γ and R points, consistent with previous literature. These band crossings lead to four extended Fermi arcs on the (001) surface termination, with extremely rich and complex connectivity behavior.

The non-symmorphic skew-rotation symmetries inherent to space group $P2_13$ also permit the presence of unpaired WPs: topological crossings without counterparts of opposite chirality. In this case, the topological charge is compensated by nodal surfaces pinned at the BZ boundaries due to time-reversal symmetry. We identified many of these points close to the Fermi level and studied their behavior under hydrostatic pressure up to 3 GPa. We also pointed out that the charge-2 Dirac point at M represents an example of such isolated crossings.

Motivated by the experimental evidence for multi-gap superconductivity in BeAu and theoretical works on s_{\pm} pairing in B20 compounds, we computed the Chern numbers of each Fermi surface sheet. We determined that the

sheets surrounding the multifold fermions at Γ and R indeed carry Chern numbers of ± 4 , consistent with a $\nu = 4$ topological superconducting phase [21]. In the course of our analysis, we also discovered a large Fermi surface region carrying a Chern number of $+6$, the highest reported for a single Fermi sheet. This suggests the potential for a $\nu = 6$ topological phase, although its realization remains unlikely. However, similar Fermi surfaces are shared by many other B20 compounds (like the fellow superconductor RhGe), making our study of broader relevance. Additionally, independent of superconductivity, the existence of such high Chern number Fermi surfaces may have implications for transport responses beyond those seen in classical Weyl systems.

Finally, our atomic-projected band structure analysis revealed a significant difference in the orbital composition of the Fermi pocket around M compared other states at the Fermi level, with the former showing a much stronger Be character. Given that superconductivity in BeAu is likely enhanced by Be-based electron-phonon coupling, this insight could be important for understanding the origin of its multi-gap superconducting behavior.

VII. ACKNOWLEDGEMENTS

We thank Eteri Svanidze for stimulating discussions and Ulrike Nitzsche for technical assistance. This work was supported by the Deutsche Forschungsgemeinschaft (DFG, German Research Foundation) under Germany's Excellence Strategy through the Würzburg-Dresden Cluster of Excellence on Complexity and Topology in Quantum Matter – *ct.qmat* (EXC 2147, project-ids 390858490, 392019). M.G.V. thanks support to PID2022-142008NB-I00 project funded by MICIU/AEI/10.13039/501100011033 and FEDER, UE, and Canada Excellence Research Chairs Program for Topological Quantum Matter. D. V. received funding from the National Research, Development and Innovation Office of Hungary under OTKA grant no. FK 146499, and the János Bolyai Research Scholarship of the Hungarian Academy of Sciences.

-
- [1] X. Wang, C. Yi, and C. Felser, Chiral Quantum Materials: When Chemistry Meets Physics, *Adv. Mater.* **36**, 2308746 (2024).
 - [2] K. Alpin, M. M. Hirschmann, N. Heinsdorf, A. Leonhardt, W. Y. Yau, X. Wu, and A. P. Schnyder, Fundamental laws of chiral band crossings: Local constraints, global constraints, and topological phase diagrams, *Phys. Rev. Res.* **5**, 043165 (2023).
 - [3] B. Bradlyn, J. Cano, Z. Wang, M. G. Vergniory, C. Felser, R. J. Cava, and B. A. Bernevig, Beyond dirac and weyl fermions: Unconventional quasiparticles in conventional crystals, *Science* **353**, aaf5037 (2016).
 - [4] I. Robredo, N. B. M. Schröter, C. Felser, J. Cano, B. Bradlyn, and M. G. Vergniory, Multifold topological semimetals, *EPL* **147**, 46001 (2024).
 - [5] J. A. Krieger, S. Stolz, I. Robredo, K. Manna, E. C. McFarlane, M. Date, B. Pal, J. Yang, E. B. Guedes, J. H. Dil, C. M. Polley, M. Leandersson, C. Shekhar, H. Borrmann, Q. Yang, M. Lin, V. N. Strocov, M. Caputo, M. D. Watson, T. K. Kim, C. Cacho, F. Mazzola, J. Fujii, I. Vobornik, S. S. P. Parkin, B. Bradlyn, C. Felser, M. G. Vergniory, and N. B. M. Schröter, Weyl spin-momentum locking in a chiral topological semimetal, *Nat. Comm.* **15**, 3720 (2024).
 - [6] F. de Juan, A. G. Grushin, T. Morimoto, and J. E. Moore, Quantized circular photogalvanic effect in Weyl semimetals, *Nat. Comm.* **8** (2017).
 - [7] B. Lu, S. Sayyad, M. A. Sánchez-Martínez, K. Manna, C. Felser, A. G. Grushin, and D. H. Torchinsky, Second-harmonic generation in the topological multifold semimetal RhSi, *Phys. Rev. Res.* **4**, L022022 (2022).
 - [8] F. Flicker, F. de Juan, B. Bradlyn, T. Morimoto, M. G. Vergniory, and A. G. Grushin, Chiral optical response of multifold fermions, *Phys. Rev. B* **98**, 155145 (2018).
 - [9] J. Ahn and B. Ghosh, Topological Circular Dichroism in Chiral Multifold Semimetals, *Phys. Rev. Lett.* **131**, 116603 (2023).
 - [10] I. Robredo, P. Rao, F. de Juan, A. Bergara, J. L. Mañes, A. Cortijo, M. G. Vergniory, and B. Bradlyn, Cubic hall viscosity in three-dimensional topological semimetals, *Phys. Rev. Res.* **3**, L032068 (2021).
 - [11] N. N. Orlova, A. V. Timonina, N. N. Kolesnikov, and E. V. Deviatov, Gate-Dependent Nonlinear Hall Effect at Room Temperature in Topological Semimetal GeTe, *Chin. Phys. Lett.* **40** (2023).
 - [12] Z. Ni, B. Xu, M.-A. Sanchez-Martinez, Y. Zhang, K. Manna, C. Bernhard, J. W. F. Venderbos, F. de Juan, C. Felser, A. G. Grushin, and L. Wu, Linear and nonlinear optical responses in the chiral multifold semimetal RhSi, *npj Quantum Mater.* **5**, 96 (2020).
 - [13] W. Wu, Y. Liu, S. Li, C. Zhong, Z.-M. Yu, X.-L. Sheng, Y. X. Zhao, and S. A. Yang, Nodal surface semimetals: Theory and material realization, *Phys. Rev. B* **97**, 115125 (2018).
 - [14] Z.-M. Yu, W. Wu, Y. X. Zhao, and S. A. Yang, Circumventing the no-go theorem: A single Weyl point without surface Fermi arcs, *Phys. Rev. B* **100**, 041118 (2019).
 - [15] J.-Z. Ma, Q.-S. Wu, M. Song, S.-N. Zhang, E. B. Guedes, S. A. Ekahana, M. Krivenkov, M. Y. Yao, S.-Y. Gao, W.-H. Fan, T. Qian, H. Ding, N. C. Plumb, M. Radovic, J. H. Dil, Y.-M. Xiong, K. Manna, C. Felser, O. V. Yazyev, and M. Shi, Observation of a singular Weyl point surrounded by charged nodal walls in PtGa, *Nat. Comm.* **12**, 3994 (2021).
 - [16] X.-L. Qi, T. L. Hughes, and S.-C. Zhang, Topological invariants for the Fermi surface of a time-reversal-invariant superconductor, *Phys. Rev. B* **81**, 134508 (2010).
 - [17] P. Hosur, X. Dai, Z. Fang, and X.-L. Qi, Time-reversal-invariant topological superconductivity in doped Weyl

- semimetals, *Phys. Rev. B* **90**, 045130 (2014).
- [18] S. Mardanya, M. Kargarian, R. Verma, T.-R. Chang, S. Chowdhury, H. Lin, A. Bansil, A. Agarwal, and B. Singh, Unconventional superconducting pairing in a B20 multifold Weyl fermion semimetal, *Phys. Rev. Mater.* **8**, L091801 (2024).
- [19] Y. Huang, Topological superconductivity in superconducting chiral topological semimetals with parallel spin-momentum locking (2024), arXiv:2408.00202 [cond-mat.supr-con].
- [20] C. Lee, C. Yoon, T. Kim, S. B. Chung, and H. Min, Topological multiband *s*-wave superconductivity in coupled multifold fermions, *Phys. Rev. B* **104**, L241115 (2021).
- [21] Y. Huang and S.-K. Jian, Three-dimensional time reversal invariant topological superconductivity in doped chiral topological semimetals, *Phys. Rev. B* **103**, L161113 (2021).
- [22] A. Amon, E. Svanidze, R. Cardoso-Gil, M. N. Wilson, H. Rosner, M. Bobnar, W. Schnelle, J. W. Lynn, R. Gumeniuk, C. Hennig, G. M. Luke, H. Borrmann, A. Leithe-Jasper, and Y. Grin, Noncentrosymmetric superconductor BeAu, *Phys. Rev. B* **97**, 014501 (2018).
- [23] J. Beare, M. Nugent, M. N. Wilson, Y. Cai, T. J. S. Munsie, A. Amon, A. Leithe-Jasper, Z. Gong, S. L. Guo, Z. Guguchia, Y. Grin, Y. J. Uemura, E. Svanidze, and G. M. Luke, μ SR and magnetometry study of the type-I superconductor BeAu, *Phys. Rev. B* **99**, 134510 (2019).
- [24] D. Singh, A. D. Hillier, and R. P. Singh, Type-I superconductivity in the noncentrosymmetric superconductor BeAu, *Phys. Rev. B* **99**, 134509 (2019).
- [25] A. Tsvyashchenko, V. Sidorov, A. Petrova, L. Fomicheva, I. Zibrov, and V. Dmitrienko, Superconductivity and magnetism in noncentrosymmetric RhGe, *Journal of Alloys and Compounds* **686**, 431 (2016).
- [26] R. Khasanov, R. Gupta, D. Das, A. Amon, A. Leithe-Jasper, and E. Svanidze, Multiple-gap response of type-I noncentrosymmetric BeAu superconductor, *Phys. Rev. Res.* **2**, 023142 (2020).
- [27] R. Khasanov, R. Gupta, D. Das, A. Leithe-Jasper, and E. Svanidze, Single-gap versus two-gap scenario: Specific heat and thermodynamic critical field of the noncentrosymmetric superconductor BeAu, *Phys. Rev. B* **102**, 014514 (2020).
- [28] S. Datta, A. Vasdev, P. S. Rana, K. Motla, A. Kataria, R. P. Singh, T. Das, and G. Sheet, Spectroscopic evidence of multigap superconductivity in noncentrosymmetric AuBe, *Phys. Rev. B* **105**, 104505 (2022).
- [29] R. Khasanov, R. Vocaturo, O. Janson, A. Koitzsch, R. Gupta, D. Das, N. P. M. Casati, M. G. Vergniory, J. van den Brink, and E. Svanidze, Influence of pressure on the properties of the multigap type-I superconductor BeAu, *Phys. Rev. B* **111**, 104507 (2025).
- [30] A. Bhowmick, J. Singh, and V. Kanchana, Spin Hall conductivity, magnetoresistance, and nontrivial topology in BeAu, *Phys. Rev. B* **111**, 115122 (2025).
- [31] V. E. Dmitrienko, Quasicrystals and their approximants: dodecahedral local ordering versus canonical-cell description, *Acta Crystallogr. A* **50**, 515–526 (1994).
- [32] K. Koepnik and H. Eschrig, Full-potential nonorthogonal local-orbital minimum-basis band-structure scheme, *Phys. Rev. B* **59**, 1743 (1999).
- [33] J. P. Perdew, K. Burke, and M. Ernzerhof, Generalized Gradient Approximation Made Simple, *Phys. Rev. Lett.* **78**, 1396 (1997).
- [34] K. Koepnik, O. Janson, Y. Sun, and J. van den Brink, Symmetry-conserving maximally projected Wannier functions, *Phys. Rev. B* **107**, 235135 (2023).
- [35] M. Yao, K. Manna, Q. Yang, A. Fedorov, V. Voroshnin, B. Valentin Schwarze, J. Hornung, S. Chattopadhyay, Z. Sun, S. N. Guin, J. Wosnitzer, H. Borrmann, C. Shekhar, N. Kumar, J. Fink, Y. Sun, and C. Felser, Observation of giant spin-split Fermi-arc with maximal Chern number in the chiral topological semimetal PtGa, *Nat. Comm.* **11**, 2033 (2020).
- [36] G. Chang, S.-Y. Xu, B. J. Wieder, D. S. Sanchez, S.-M. Huang, I. Belopolski, T.-R. Chang, S. Zhang, A. Bansil, H. Lin, and M. Z. Hasan, Unconventional Chiral Fermions and Large Topological Fermi Arcs in RhSi, *Phys. Rev. Lett.* **119**, 206401 (2017).
- [37] D. S. Sanchez, T. A. Cochran, I. Belopolski, Z.-J. Cheng, X. P. Yang, Y. Liu, T. Hou, X. Xu, K. Manna, C. Shekhar, J.-X. Yin, H. Borrmann, A. Chikina, J. D. Denlinger, V. N. Strocov, W. Xie, C. Felser, S. Jia, G. Chang, and M. Z. Hasan, Tunable topologically driven Fermi arc van Hove singularities, *Nat. Phys.* **19**, 682–688 (2023).
- [38] A. Kuibarov, O. Suvorov, R. Vocaturo, A. Fedorov, R. Lou, L. Merkwitz, V. Voroshnin, J. I. Facio, K. Koepnik, A. Yaresko, G. Shipunov, S. Aswartham, J. van den Brink, B. Büchner, and S. Borisenko, Evidence of superconducting Fermi arcs, *Nature* **626**, 294–299 (2024).
- [39] M. Trama, V. Könye, I. C. Fulga, and J. van den Brink, Self-consistent surface superconductivity in time-reversal symmetric weyl semimetals, *Phys. Rev. B* **112**, 064514 (2025).
- [40] A. Nomani and P. Hosur, Intrinsic surface superconducting instability in type-I Weyl semimetals, *Phys. Rev. B* **108**, 165144 (2023).
- [41] X. Bai, W. LiMing, and T. Zhou, Superconductivity in Weyl semimetals with time reversal symmetry, *New J. Phys.* **27**, 013003 (2025).
- [42] A. Kuibarov, S. Changdar, R. Vocaturo, O. Suvorov, A. Fedorov, R. Lou, M. Krivenkov, L. Harnagea, S. Wurmehl, J. van den Brink, B. Büchner, and S. Borisenko, Three prerequisites for high-temperature superconductivity in t-PtBi₂ (2025), arXiv:2509.02178 [cond-mat.supr-con].
- [43] F. D. M. Haldane, Berry Curvature on the Fermi Surface: Anomalous Hall Effect as a Topological Fermi-Liquid Property, *Phys. Rev. Lett.* **93**, 206602 (2004).